AGU PUBLICATIONS

JGR

Journal of Geophysical Research: Atmospheres

RESEARCH ARTICLE
10.1002/2014JD022879

Lidar observations of gravity wave activity in the middle atmosphere over Davis (69°S, 78°E), Antarctica

B. Kaifler[1,2], F.-J. Lübken[2], J. Höffner[2], R. J. Morris[3], and T. P. Viehl[2]

[1]Institute of Atmospheric Physics, German Aerospace Center, Oberpfaffenhofen, Germany, [2]Leibniz Institute of Atmospheric Physics, Rostock University, Kühlungsborn, Germany, [3]Australian Antarctic Division, Kingston, Tasmania, Australia

Key Points:
- Gravity wave signatures are extracted from lidar data
- Gravity wave activity in the Antarctic middle atmosphere is characterized
- Critical-level filtering of gravity waves is investigated

Correspondence to:
B. Kaifler,
bernd.kaifler@dlr.de

Citation:
Kaifler, B., F.-J. Lübken, J. Höffner, R. J. Morris, and T. P. Viehl (2015), Lidar observations of gravity wave activity in the middle atmosphere over Davis (69°S, 78°E), Antarctica, *J. Geophys. Res. Atmos.*, *120*, 4506–4521, doi:10.1002/2014JD022879.

Received 19 NOV 2014
Accepted 10 APR 2015
Accepted article online 20 APR 2015
Published online 19 MAY 2015

Abstract A 16 month series of lidar measurements in the stratosphere and mesosphere-lower thermosphere (MLT) region over Davis Station (69°S, 78°E) in Antarctica is used to study gravity waves. The unprecedentedly large number of observations totaling 2310 h allows us to investigate seasonal variations in gravity wave activity in great detail. In the stratosphere the gravity wave potential energy density (GWPED) is shown to have a large seasonal variation with a double peak in winter and minimum in summer. We find conservative wave propagation to occur between 29 and 41 km altitude in winter as well as in summer, whereas smaller energy growth rates were observed in spring and autumn. These results are consistent with selective critical-level filtering of gravity waves in the lower stratosphere. In the MLT region the GWPED is found to have a semiannual oscillation with maxima in winter and summer. The structure of the winter peak is identical to that in the stratosphere, suggesting that the gravity wave flux reaching the MLT region is controlled by the wind field near the tropopause level.

1. Introduction

Atmospheric gravity waves are important for vertical coupling in the atmosphere. They transport energy and momentum vertically and horizontally over large distances. At high latitudes, dissipation of these waves in the mesosphere-lower thermosphere region (hereafter MLT region) transfers momentum into the background flow, driving a global meridional circulation from the summer pole to the winter pole [*Lindzen*, 1981; *Holton*, 1983]. Associated with this circulation is the upwelling of air at the summer pole causing the strong adiabatic cooling of the summer MLT region [*Andrews et al.*, 1987; *Becker*, 2012]. This gravity wave-induced cooling gives rise to observed temperatures as low as 130 K which are far from radiative equilibrium [*Lübken*, 1999; *Lübken et al.*, 2014]. For this reason, phenomena like noctilucent clouds and polar mesospheric summer echoes are limited to the summer polar region [*Olivero and Thomas*, 1986]. Without gravity wave-induced cooling, temperatures in the summer MLT remain above the frost point [*Rapp and Thomas*, 2006]. The occurrence of noctilucent clouds is thus a result of gravity waves propagating from the troposphere/lower stratosphere into the MLT region.

Gravity waves have been extensively studied in models [e.g., *Zhang*, 2004] as well as through employing observational techniques such as lidars [e.g., *Rauthe et al.*, 2008; *Yamashita et al.*, 2009], radars [e.g., *Nicolls et al.*, 2010; *Lue et al.*, 2013], radiosondes [e.g., *Allen and Vincent*, 1995; *Moffat-Griffin et al.*, 2011], satellite-based radiometers [e.g., *Alexander et al.*, 2008; *Wright and Gille*, 2013], and Global Positioning System radio occultation [e.g., *Wang and Alexander*, 2010]. Among all observational techniques, lidars provide the highest temporal and vertical resolutions over a wide altitude range and observation periods up to several days.

Lidar observations in the Antarctic region are rare due to the difficulties involved in setting up and operating complex optical instruments in such a harsh environment. First, lidar-based measurements of gravity waves on the Antarctic continent were reported by *Nomura et al.* [1989]. *Nomura et al.* [1989] used a sodium lidar located at Syowa Station (69°S, 40°E) in 1985 to derive gravity wave parameters from density perturbations in the sodium layer (approximately 80–105 km). *Collins and Gardner* [1995] studied gravity waves observed in 1990 at the South Pole in the sodium layer and in stratospheric clouds between 15 and 30 km. An iron Boltzmann/Rayleigh lidar was used to investigate gravity waves in 30–45 km altitude at the South Pole and at Rothera between 2000 and 2005 [*Yamashita et al.*, 2009]. This instrument was later moved to McMurdo (78°N, 167°E) [*Chen et al.*, 2013]. A Rayleigh lidar providing temperature profiles for gravity wave studies between 30 and 70 km has been operational at Davis (69°N, 78°E) since 2001 [*Klekociuk et al.*, 2003; *Alexander et al.*, 2011].

Table 1. Statistics of the Lidar Observations

	Year	Jan	Feb	Mar	Apr	May	Jun	Jul	Aug	Sep	Oct	Nov	Dec	Total
Observations	2011	11	4	5	7	4	8	4	7	4	6	5	9	
Observation hours		185.8	128.8	71.8	121.8	97.0	260.3	124.8	213.0	108.5	183.3	189.0	215.3	
Observations	2012	8	3	5	5									95
Observation hours		166.8	108.3	64.8	71.5									2310.3

Finally, in December 2010 the Leibniz Institute of Atmospheric Physics (IAP) iron Doppler lidar was installed at Davis Station and took data until December 2012 [*Lübken et al.*, 2014]. This lidar was capable of measuring gravity waves in the iron layer (approximately 80–100 km) and between 30 and 50 km. As distinguished from all previous lidars in Antarctica, the IAP lidar was operated during a full annual cycle achieving on average 158 observation hours per month. The resulting data set is the largest high-resolution temperature data set to date. In this work we report on gravity analysis using this data set.

2. Lidar System, Observations, and Analysis

The IAP mobile iron lidar is a mesospheric lidar system designed to probe the Doppler-broadened resonance line of iron at 386 nm wavelength to measure atmospheric temperature profiles in the MLT region [*Lautenbach and Höffner*, 2004]. It uses a frequency-doubled Alexandrite ring laser as light source operating at 33 Hz pulse repetition rate. Emitted pulse energies are 30 mJ in the UV (386 nm) and 100 mJ in the IR (772 nm). The receiver comprises a telescope with 80 cm aperture and a narrow field of view of 66 μrad, a double-etalon narrow-band filter for each of the two wavelengths, and photon detectors operated in single photon counting mode. Photon count profiles with 25 m vertical resolution are stored for each individual laser pulse. The lidar system is capable of measuring atmospheric temperatures in full daylight with a typical uncertainty of 1–5 K in the MLT region (approximately 80–100 km altitude) after 1 h integration and binning to 2 km vertical resolution. Stratospheric temperatures with 1 km vertical resolution and 1 h integration time are retrieved between 25 and 60 km altitude with typical uncertainties ranging from approximately 7 K at 55 km altitude to less than 2 K below 40 km altitude. Higher vertical and temporal resolutions are possible for lidar measurements acquired in darkness.

The lidar system was operated at the Australian Antarctic station Davis (68.58°S, 77.97°E) between December 2010 and December 2012 for more than 2600 h. Thus, the lidar measurements form the most extensive high-resolution middle atmosphere temperature data set available to date. This data set covers a full annual cycle with approximately equal sampling and is therefore well suited for studying seasonal variations of, e.g., temperature and gravity wave activity. Because no lidar observations were acquired in austral winter 2012, we limited our gravity wave study presented here to the period January 2011 to April 2012. Also, we discarded all lidar observations shorter than 6 h in order to guarantee sampling of at least one half-period of long-period inertia gravity waves (the Coriolis parameter for the location of Davis Station is approximately 12.7 h). Monthly statistics of the resulting subset of lidar observations (2310 h in total) are listed in Table 1. With more than 260 h, the largest number of observation hours per month was achieved in June 2011. This number corresponds to an average of 8.7 h of lidar observations per day or 37% of the total time. Considering the 16 month period selected for this study, the average observation period per day is 4.8 h or about 20% of the total time.

In this work we characterize gravity waves by wave-induced temperature perturbations $T'(z,t)$ and gravity wave potential energy densities (from now on referred to as GWPED), E_p, defined as

$$E_p(z) = \frac{1}{2}\frac{g^2}{\overline{N^2(z,t)}}\overline{\left(\frac{T'(z,t)}{T_0(z,t)}\right)^2}, \tag{1}$$

where g is the gravitational acceleration, equal to approximately 9.7 m s^{-2}; T_0 is the undisturbed background temperature; and z and t denote altitude and time, respectively. The squared buoyancy frequency N^2 is calculated from temperature profiles using the relation

$$N^2(z,t) = \frac{g}{T_0(z,t)}\left(\frac{\partial T_0(z,t)}{\partial z} + \frac{g}{c_p}\right), \tag{2}$$

where c_p is the specific heat at constant pressure, equal to 1004 J K^{-1} kg^{-1}. Overbars in equation (1) denote temporal averages with regard to the duration of the lidar observation of typically 19 h.

Several methods for deriving wave-induced perturbations $T'(z,t)$ from the original lidar measurements $T(z,t)$ have been devised and used in the past. *Gerrard et al.* [2004] computed background density profiles based on a third-order polynomial fit to measured atmospheric density profiles. The fit was then subtracted from the measured profile, and the residuals were low-pass filtered. Finally, the resulting filtered residuals were added to the fit to form the undisturbed background profile. *Yamashita et al.* [2009] took a similar approach except that they used a fifth-order polynomial, while *Rauthe et al.* [2008] extracted wave-induced temperature perturbations in the time domain by subtracting the nightly mean from measured profiles. *Duck et al.* [2001] and more recently *Alexander et al.* [2011] determined the background profile from a series of fits with a third-order polynomial. In contrast to techniques mentioned above, *Duck et al.* [2001] limited fits to a certain height window which is shifted vertically in each cycle. The background profile is then obtained by computing the weighted average of all fits. We consider this method as most reliable for extracting gravity waves given that the alternatives are generally most sensitive to waves with periods comparable to the averaging period. For example, subtraction of the nightly mean [e.g., *Rauthe et al.*, 2008] favors waves with periods in the order of the length of the observations, which range from 3 to 12 h. While in the former case (3 h) extracted gravity wave perturbations are biased toward short-period waves, disturbances from, e.g., tides and planetary waves may be falsely identified as gravity waves in the latter case (12 h). The polynomial fit method described in *Duck et al.* [2001] does not suffer from this problem because the response function in the range of relevant gravity wave periods is mostly flat.

Following the approach used by *Alexander et al.* [2011], we resampled the measured stratospheric temperature profiles with 2 km vertical resolution. Mean statistical uncertainties of the 1 h × 2 km profiles $T(z,t)$ are 2.8 K at 50 km and 0.5 K at 30 km altitudes. We note that biases in the temperature retrieval resulting from, e.g., aerosol scattering in the lower stratosphere and inaccuracies in the treatment of the narrowband optical filters may be larger. These biases are, however, approximately constant over the duration of typical lidar observations and can therefore be regarded as modification of the background temperature profile. For this reason, wave-induced temperature perturbation profiles $T'(z,t)$ calculated as

$$T'(z,t) = T(z,t) - T_0(z,t) \tag{3}$$

are not sensitive to biases, and statistical uncertainties (photon noise) are the main error source in the gravity wave analysis.

To extract the background temperature $T_0(z,t)$ from the observed temperature $T(z,t)$, we employ the method which is described in detail by *Alexander et al.* [2011] and *Duck et al.* [2001]. The following is a short summary: The observed profile $T(z,t)$ is split into overlapping segments of 20 km vertical extent, where the lower end of each segment is shifted by 2 km in altitude relative to the previous segment. Next, a third-order polynomial is fitted to each segment, and $T_0(z,t)$ is calculated as weighted average of all fits. The weights are distributed as follows: The central four bins of the fitted polynomial are weighted fully, while the contribution of the lower and upper three bins is smoothly reduced to zero toward the ends of each segment by decreasing the weights exponentially with an *e*-folding length of 3 km. This weighting scheme reduces the discontinuities which may arise from the fits wagging at the endpoints. The resulting profile is smoothed by applying a 6 km averaging filter. We call the result the background profile $T_0(z,t)$. Finally, the wave-induced perturbations $T'(z,t)$ are derived by subtracting the background profile from the measured profile (equation (3)).

Although the sensitivity of the wave extraction procedure described above drops significantly for waves with vertical wavelengths λ_z larger than 20 km (a careful analysis is presented in *Duck et al.* [2001]), $T'(z,t)$ may still contain remains from planetary waves or tides (typical $\lambda_z > 30$ km). In order to isolate the gravity wave-induced perturbations, we filter $T'(z,t)$ in the vertical domain with a high-pass filter. By choosing a cutoff wavelength of 20 km, most gravity wave signatures present in $T'(z,t)$ are retained while background effects such as tides are sufficiently suppressed. Changes in $T'(z,t)$ caused by filtering are typically in the order of 10% or less. Note that perturbations are not bandlimited in the time domain. The vertical filtered $T'(z,t)$ were then used to compute GWPED profiles according to equation (1). The overbar in equation (1) denotes the temporal average over the duration of the lidar observation (typically 19 h). We call this average the "observational mean" in analogy to the "nightly mean" which is often used in studies based on lidar data

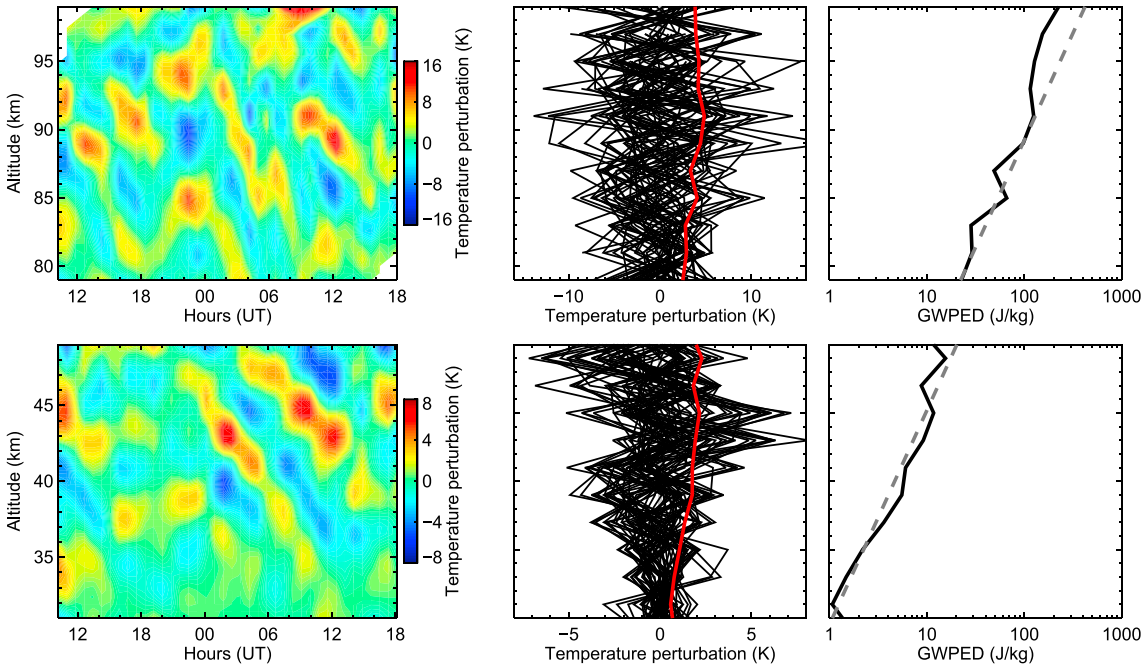

Figure 1. Illustration of data processing for gravity waves on 15/16 August 2011. (left column) Temperature perturbations in time. (middle column) Hourly perturbation profiles (black) and mean perturbation profile (red). (right column) Mean gravity wave potential energy density GWPED profile (solid line) and conservative growth rate (dashed line).

acquired with lidar instruments which are not capable of observing in daylight conditions. In this study we divided the gravity wave analysis in two sections: First, we analyzed Rayleigh temperature profiles which are typically retrieved between 25 and 60 km altitude. In a second step we analyzed iron Doppler temperature measurements between approximately 80 and 100 km. Extraction of GWPED profiles from our mesospheric temperature data is, however, complicated by the fact that the iron layer shows strong seasonal variations in layer width and metal density [*Gardner et al.*, 2011]. As the iron lidar can measure iron temperature only in altitude regions where the iron density is sufficiently high, the upper and lower ends of the temperature profiles are affected by variations of the iron layer. Especially in summer when the iron density reaches the annual minimum, the length of the retrieved temperature profile often falls below the minimum of 20 km required by the gravity wave extraction procedure, and no GWPED profiles can be obtained. For this reason, in our data set mean GWPED in the summer mesosphere is less reliable than in winter, contrary to statistics of observation hours (Table 1).

Figure 1 shows gravity wave signatures extracted from 32 h of lidar observations on 15/16 August 2011. In the stratosphere, large wave amplitudes occurred during the first 4 h followed by a relatively quiet period from about 1400 UT to midnight. Then gravity wave amplitudes increased again and remained at this level for the remainder of the observation period. In contrast, no such distinct temporal variation in amplitude is visible at mesospheric altitudes. The mean vertical wavelength is approximately 9 km in both cases, and observed wave periods range from 4 to 10 h. Phase progression was predominantly downward, implying upward transport of energy. As evident from Figure 1 (middle column), hourly perturbation amplitudes range from approximately 0.5 K in amplitude at 30 km altitude to the maximum of 15 K in 89–94 km altitude (note the different color scale). Mean perturbation amplitudes are generally about 50% smaller. Typical values are 0.3–2 K in the stratosphere and 3–5 K in the mesosphere.

Figure 1 (right column) shows mean GWPED profiles computed according to equation (1). Note the different growth rates of T' and GWPED. As the energy density is proportional to the square of the perturbation amplitudes, the GWPED increases with height more quickly than T'. On 15/16 August 2011, the GWPED increased proportional to $\exp(z/H)$ up to approximately 45 km, where H is the density scale height of the atmosphere. For reference, the growth rate of the exponential $\exp(z/6.8\text{km})$ is also shown, with $H = 6.8$ km being a typical value for the density scale height in the stratosphere. The steady increase in GWPED is indicative of freely propagating gravity waves, while the reduced growth rate observed above 45 km may be associated with wave

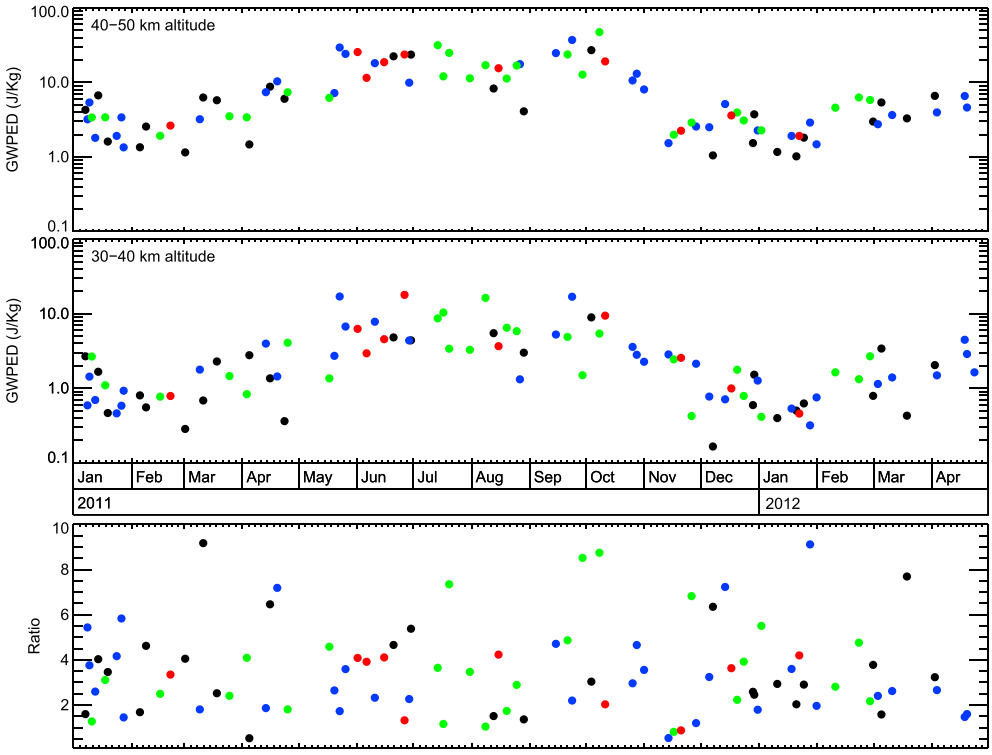

Figure 2. GWPED at (top) 40–50 km altitude and (middle) 30–40 km altitude; (bottom) GWPED ratio. Color indicates the length of the lidar observation: black: 6–12 h, blue: 12–24 h, green: 24–48 h, and red: >48 h.

breaking. Given the large variability of temperature perturbations, we note that based on the single observation shown in Figure 1, the observed decrease in GWPED above 45 km may not be significant. However, we will present seasonal averages which clearly show a significant decrease in section 3.2.

Similar behavior is observed in the mesosphere: The GWPED increases exponentially between 79 and 91 km altitude, implying conservative wave propagation in this region. Above, the growth rate is distinctly smaller but still positive. At first glance this seems to be contradictory to the mean temperature perturbation profile which shows a clear decline above 91 km. However, we need to keep in mind the influence of the background atmosphere in order to understand propagation of gravity waves. On 15/16 August 2011, the atmosphere was nearly isothermal between 79 and 91 km, implying a constant buoyancy frequency in this region, while at higher altitudes the temperature decreased rapidly toward the mesopause at approximately 100 km. The negative temperature gradient reduces the buoyancy frequency according to equation (2), and this in turn leads to an increase in GWPED despite decreasing temperature perturbation amplitudes. In the following sections we use GWPED to analyze and interpret the gravity wave activity over Davis Station.

3. Gravity Wave Activity in the Stratosphere

3.1. Short-Term and Seasonal Variation

Measurements of gravity waves in the stratosphere are typically available between 28 and 50 km. To study vertical propagation, we divided the altitude range into two altitude regions 30–40 km and 40–50 km. For each of the two regions we calculated the observational mean assuming a lognormal distribution of GWPED values.

Figure 2 shows the GWPED for the two altitude regions, each of the dots representing a single lidar observation. It is evident from this figure that there is significant short-term variability, i.e., from one lidar observation to the next few days later. On this time scale, GWPED values can vary by as much as half an order of magnitude, whereas the typical variation is in the order of 100%. It is important to note that this variability is of geophysical origin and not related to problems with the lidar instrument, as photon noise and other instrumental effects amount to typical uncertainties in GWPED of less than 10%. Though sampling of single large-amplitude gravity wave may contribute to the variability, we believe that sampling effects are sufficiently reduced as a result

Table 2. Relative Mean Variability of GWPED, $\overline{q_x}$, for Two Altitude Regions[a]

x (days)	4	6	8	10	20	40
$\overline{q_x}$ 40–50 km (%)	41	38	38	37	39	47
$\overline{q_x}$ 30–40 km (%)	58	56	53	53	57	64

[a]The index x specifies the analyzing period in days. See text for details.

of the long observation periods. Even for long-period inertia gravity waves, it is reasonable to expect a minimum of two to three wave maxima and minima within the mean observation period of 24.3 h. This guarantees realistic estimates of mean T'. In contrast, short observations of, e.g., less than 6 h may sample only one half or one third of a wave period leading to underestimates in mean T' (GWPED).

To quantify the variability on short time scales, we introduce a quantity termed "mean relative variability" $\overline{q_x}$, where the index x specifies the analyzing period. The $\overline{q_x}$ values are computed as follows: A time interval of x days is formed for each lidar observation centered at the observation time. Next, the mean $\overline{E_p}$ and the standard deviation σ_{E_p} of all observational means within the time interval is computed. Finally, $\overline{q_x}$ is found by averaging all ratios $\sigma_{E_p}/\overline{E_p}$. Results for analyzing periods between 4 and 40 days are listed in Table 2. The most striking feature is a significant difference in short-term variability in the two altitude regions. For all analyzing periods up to 40 days, the variability at lower altitudes is larger, e.g., 35% in 40–50 km versus 53% in 30–40 km altitude. The absolute difference is approximately constant (8 days: 15% and 20 days: 18%), and there is no significant correlation with the length of the analyzing period.

Comparing q_x values at fixed altitudes reveals another interesting characteristic of the short-term variability: Starting with short analyzing periods, the relative variability decreases with increasing averaging intervals and reaches a minimum at 8–10 days. For longer periods the variability increases again. Latter increase is mainly attributed to large-amplitude seasonal variations becoming increasingly dominant over short-term variations, while the initial decrease is likely a statistical effect. The mean number of observations per 4 day period is 2.2; i.e., there are only two observations for the majority of the intervals. Such small sample populations introduce a significant bias in estimates of q_x. Hence, we conclude that q_x values in the range of 8–10 days represent the most reliable estimate for characterization of the short-term variability of gravity waves. We tested against possible influences of the observation length on GWPED estimates by computing correlations. We fist remove seasonal variations by subtracting the time series smoothed with a 30 day Hann filter from the original time series. The correlation coefficient obtained from correlating the reduced time series with the length of individual observations is found to be 0.005 at 40–50 km and 0.004 at 30–40 km. We conclude that the length of the observation has negligible influence.

In addition to variations on time scales of few days, the GWPED observations in Figure 2 show also a clear annual oscillation with low gravity wave activity in austral summer and large GWPED values in austral winter. To study this oscillation in more detail, we computed monthly means for both altitude regions assuming a lognormal distribution. Figure 3 shows the monthly means as well as the standard deviation of the means. In the lower altitude band (30–40 km altitude) small GWPED values occur in December and January with 1.0 J/kg and 0.8 J/kg, respectively. The wave activity increases through austral autumn and reaches a first maximum in months May–July, followed by a small dip in August. A second maximum of equal height occurs in September/October before the wave activity falls off again in late austral spring. Maximum GWPED values were observed in July (5.9 J/kg) and October (5.4 J/kg). By comparison, the local minimum (3.9 J/kg) which occurs in August is rather distinct though still within standard deviation of the means of the surrounding months. The seasonal oscillation of the GWPED in the higher-altitude band (40–50 km altitude) is quite similar to the lower altitude band. Notable differences include a faster decrease in GWPED at the end of austral autumn (October and November) and a larger oscillation amplitude. Monthly GWPED values in 40–50 km altitude vary by a factor of 7.6 (peak to valley), while in the lower altitude band with a value of 6.6 the variation is slightly smaller.

3.2. Seasonal Profiles

In the absence of dissipation, the GWPED grows with height proportional to $\exp(z/H)$. Measured GWPED profiles matching this conservative growth rate are therefore indicative of freely propagating (conservative) waves. The reverse is, however, not necessarily true, namely, that a nonconservative growth rate implies

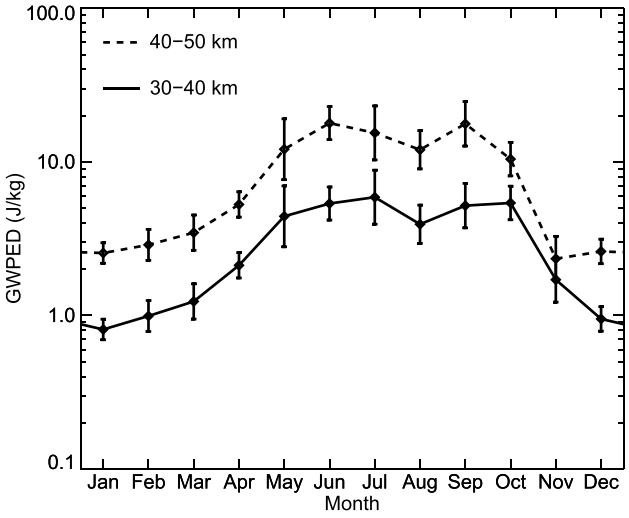

Figure 3. Seasonal variation of GWPED at 30–40 km (solid line) and 40–50 km (dashed line). Vertical bars mark the standard deviation of the mean.

energy dissipation. Under certain atmospheric conditions gravity waves can be refracted in "atmospheric waveguides" [*Fritts and Yuan*, 1989]. While gravity waves may propagate freely inside these waveguides, the GWPED profile decreases directly above the waveguide.

In order to study the vertical propagation of gravity waves as well as seasonal variations, we split our data set into four parts: summer (months January and February, 26 observations), autumn (months March and April, 22 observations), winter (months May–August, 23 observations), and remaining months (September–December) designated "transition period." The breakdown of the Antarctic vortex falls in the latter period. Because gravity wave propagation is strongly influenced by the breakdown of the vortex, we discuss the transition period in detail in the section 5.

For the remaining three seasons we computed seasonal averages and estimates of the variability defined as the standard deviation of the mean. Figure 4 shows the resulting profiles. The summer profile clearly indicates conservative wave propagation up to approximately 43 km altitude. This suggests that nearly all wave energy is carried up to this level with no or very little dissipation between 29 and 43 km. Above, the GWPED profile deviates slightly from the conservative growth rate, resulting in approximately 10% loss in GWPED at 51 km altitude. The winter profile shows characteristics similar to the summer profile. Conservative wave propagation is observed between 29 and 41 km, followed by rapidly decreasing growth rates above. At 49 km altitude, gravity waves have lost more than half of their potential energy density. Note that the seasonal variation in atmospheric temperature causes modulation of the density scale height. In winter, the temperature in the region of interest is on average 29 K lower than in summer. This temperature difference translates into a 13% decrease in scale height and hence larger conservative growth rates. The autumn GWPED profile may be considered as mixed state in between the summer profile and the winter profile. The bottom part of the profile follows approximately the conservative growth rate, while above 37 km altitude the profile converges toward the summer profile. Values above 45 km altitude are not shown because of large statistical uncertainties caused by low lidar return signal in March/April 2012.

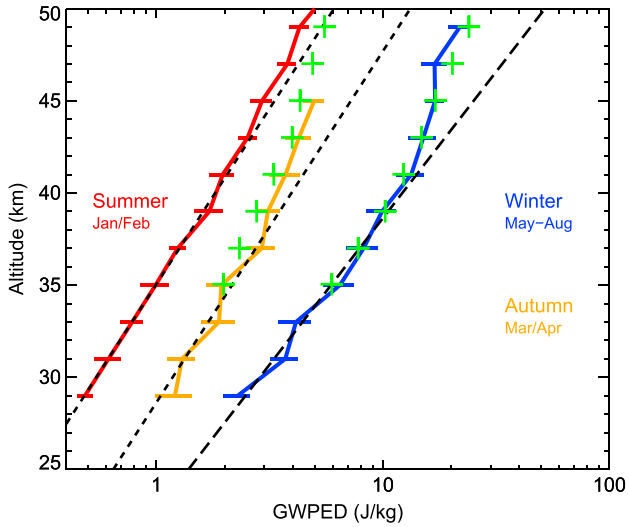

Figure 4. Vertical GWPED profiles for summer (red), autumn (orange), and winter (blue). Horizontal lines mark the standard deviation of the mean. For comparison conservative growth rates are also shown (dashed lines). Profiles marked by green crosses are taken from *Alexander et al.* [2011].

4. Gravity Wave Activity in the Mesosphere

Figure 5 shows monthly and seasonal mean GWPED profiles extracted from mesospheric temperature measurements. The vertical extent of the profiles follows closely the seasonal variation of the iron density, the largest extent of the iron layer occurring in winter. In addition to seasonal

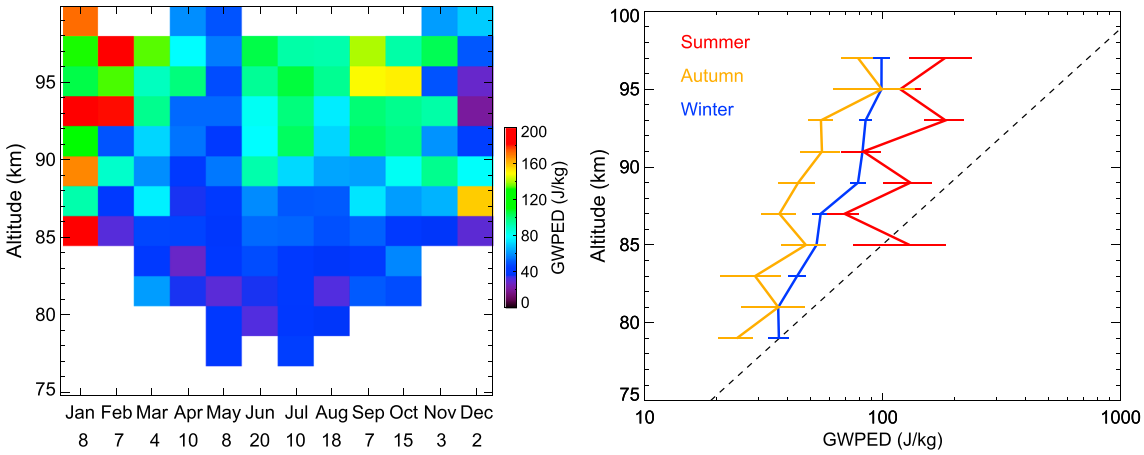

Figure 5. (left) Monthly GWPED profiles observed by the iron lidar at Davis. The number of observation per month is written below the figure. (right) Seasonal profiles with standard errors (horizontal bars). The dashed line shows the expected growth rate for conservative waves in winter scaled to the observed value at 79 km altitude.

variations, there is a substantial day-to-day variability in iron density which defines the altitude range of retrieved temperature profiles. Other prominent sources of variability include, e.g., tides and the solar effect on the layer bottom side [*Yu et al.*, 2012]. The variability described above results in retrieved temperature/GWPED profiles which vary in vertical extent from one profile to the next. Therefore, when calculating monthly mean profiles, the number of GWPED values per altitude bin may vary substantially. In order to make sure that calculated means are representative, we disregarded all data (altitude bins) where the number of observational means for a given month and altitude is less than half the maximum number for this month.

Vertical GWPED profiles in the MLT region remain well below the growth rate of conservatively propagating waves. The slopes of all three seasonal profiles in Figure 5 are roughly identical and indicate energy loss rates in the order of 80% per 10 km. We note that due to reasons given in section 2, the summer profile shows greater fluctuations, and we therefore refrain from quantitative analysis. Largest GWPED values occur in the summer months (January and February), whereas minimum values are observed in autumn (March and April). Values for December are unusual because the GWPED shows a local maximum at about 87 km altitude followed by a minimum at 94 km before the GWPED increases again further up. This profile may suggest very localized wave breaking confined to the mesopause region (about 90 km). However, there is no statistical evidence for such a conclusion, given the fact that the December profile comprises two observational means only.

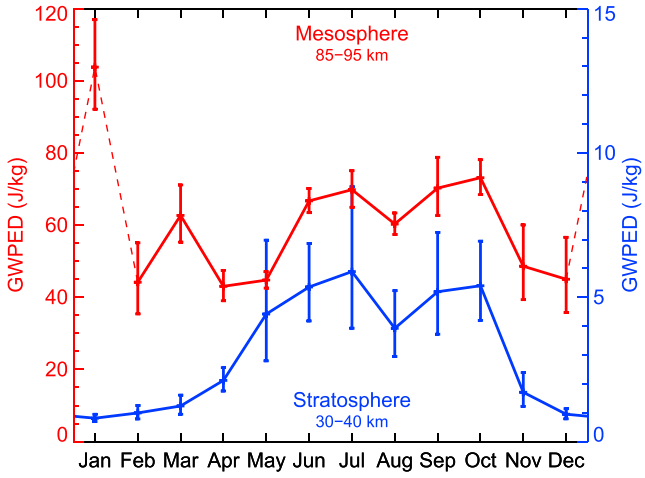

Figure 6. Seasonal variation of GWPED in the stratosphere and mesosphere. Vertical bars mark the standard deviation of the mean. Note that in winter (months May–October) values are strongly correlated.

Figure 6 shows the vertical average of monthly means. For comparison, we added the stratospheric GWPED retrieved in section 3.1. Interestingly, there appears to be a strong correlation between GWPED in the stratosphere and mesosphere as the GWPED averaged in 85–95 km shows the same double-humped structure in winter. Unlike the stratosphere, however, there is a narrower but larger secondary maximum in

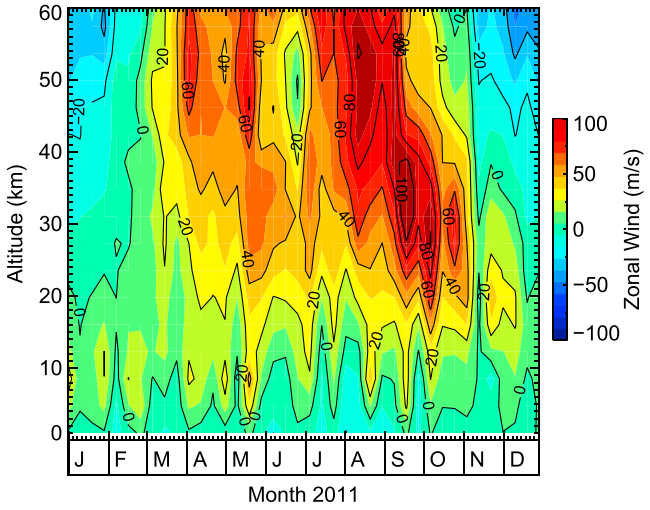

Figure 7. Zonal wind structure above Davis Station in 2011. Data are taken from the ECMWF operational analysis.

summer. The peak in January with 104 J/kg is about 50% larger than average GWPED values in winter (68 J/kg). A third maximum in March (62 J/kg) is statistically not significant.

5. Gravity Wave Filtering

At high polar latitudes the probability of gravity waves penetrating into the winter stratosphere is significantly enhanced due to the strong polar night jet which facilitates westward propagating gravity waves. Figure 7 shows the vertical structure of the zonal wind for the location of Davis Station data taken from European Centre for Medium-Range Weather Forecasts (ECMWF) operational analysis. A westerly circulation develops in the stratosphere in autumn and strengthens over the winter months, reaching wind speeds of more than 80 m/s in the upper stratosphere. This jet blocks all eastward propagating waves with the exception of waves with very large phase speeds, while westward propagating waves can reach the stratopause without hindrance. With the breakdown of the polar vortex at the end of winter, the zonal wind speed reverses. Now the path is open for eastward propagating waves while westward propagating waves are blocked. This selective filtering of gravity waves is symmetric to the winter case with regard to the direction of propagation. However, in the lower stratosphere the wind speed remains slightly positive throughout the summer months. As a consequence, waves with lower phase speeds are blocked in the summer stratosphere regardless of the direction of propagation. Because most gravity waves excited in the troposphere are expected to have small phase speeds, stratospheric GWPED in summer is also expected to be much smaller than in winter although conservative propagation of waves in the upper stratosphere may be observed in both cases. This interpretation is supported by measured GWPED profiles discussed in the previous section.

We want to study the relation between zonal wind speed and gravity wave propagation in more detail. First, we identified regions where filtering of waves with small phase speeds is expected, i.e., regions with small zonal wind speeds. For this purpose we computed daily mean profiles from ECMWF model data and selected all altitude ranges with $|u| < 2$ m/s. These ranges are marked in blue color in Figure 8. It is evident from this figure that the region where the wind reverses is progressing downward, starting at 60 km in late October and reaching approximately 25 km in December. In contrast, the second reversal in February occurs nearly instantaneously at all altitudes. Next, we computed 14 day mean GWPED profiles also shown in Figure 8. We note that due to the short averaging period, GWPED profiles are more noisy in comparison to seasonal profiles (Figure 4). However, general characteristics can still be identified. Approximately conservative wave propagation is evident in the two profiles in October up to shortly below the region of wind reversal. In November, the region moves into the altitude range where the lidar can measure GWPED, and loss of GWPED becomes more apparent. The "bulge" visible in the second November profile coincides with the location of the wind reversal. Wind filtering is even more clear in the first profile in December. The GWPED decreases strongly up to the blue shaded region, and free propagation of waves which pass through the reversal zone is observed above. In January, the region drops below the observing range of the lidar; i.e., only remaining waves with high phase speeds are visible. Because low-speed waves are filtered at the lowest altitude with low wind speed,

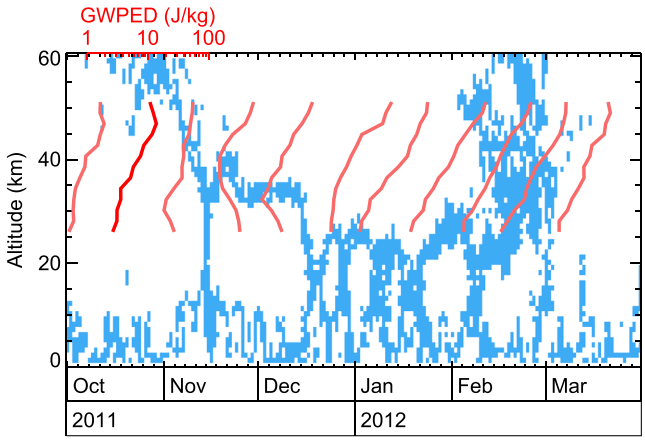

Figure 8. Interaction of gravity waves with the background wind. Blue shaded areas mark altitude ranges with $|u| < 2$ m/s (ECMWF data). Red lines show 14 day mean GWPED profiles measured by lidar. Note the strong reduction in GWPED just below the blue shaded areas in November and December.

free propagation of waves is observed throughout February even though the wind reversal zone extends over the whole observing range.

We developed a simplistic gravity wave propagation model to obtain quantitative estimates for wind filtering of gravity waves over Davis Station. In this model, waves with a given GWPED distribution in phase speed space are launched at the 12 km level and propagate upward. It is important to note that the total GWPED per unit phase speed is the primary quantity here, and we do not make any assumptions of how this energy is distributed over multiple waves with equal phase speed. In fact, we chose the energy associated with waves with a certain phase speed to be carried by a single "model wave." On first sight this seems to be a rather crude oversimplification because it is well known that the more waves are present, the more energy can be carried. However, as we are only interested in the total GWPED as function of altitude, it makes no difference whether the GWPED is distributed between few high-energy waves or many low-energy waves. To model the phase speed spectrum of gravity waves, we used a Gaussian $\propto \exp\left(-c^2/\sigma^2\right)$, where c is the phase speed and $\sigma = 8$ m/s. For reasons of simplicity, we assume a constant launch spectrum which does not vary over time. The spectrum in the range of −40 m/s to 40 m/s is partitioned into 100 bins approximately 0.8 m/s wide, and the fractional GWPED in each bin is represented by a single model wave. These 100 waves then propagate upward in vertical steps of 1 km. Wind filtering of waves is modeled by comparing in each step the phase speed of the waves with the zonal wind speed u extracted from ECMWF data. Waves are assumed to propagate freely if $|c - u| \geq 5$ m/s. In this case, the fractional GWPED is multiplied according to the conservative growth rate proportional $\exp(z/H)$, which evaluates to 1.145 for a 1 km interval. Conversely, waves are assumed to be close to a critical level if $|c - u| < 5$ m/s. Dissipation of energy is modeled by reducing the multiplication factor in three steps as listed in Table 3. We determined these factors empirically with the goal to achieving a best fit to our measurement data. By not eliminating the wave entirely, e.g., setting the multiplication factor to zero, we allow for a nonzero probability that some waves can penetrate through the critical level. These waves may in the real atmosphere originate from secondary gravity waves, come from outside the model domain, or simply represent limitations of the model, e.g., not taking into account wave-wave interactions. In a last step we integrated the modeled GWPED spectrum over phase speed at each altitude to produce a GWPED profile similar to lidar measurements. The resulting integrated profile must be scaled properly in order to convert arbitrary energy units used in model calculations to the GWPED unit J/kg. The scaling factor

Table 3. Multiplication Factors Used in the Simplistic Gravity Wave Propagation Model

Condition	Multiplication Factor
$\|c - u\| \geq 5$ m/s	1.156
2 m/s $\leq \|c - u\| < 5$ m/s	1.000
1 m/s $\leq \|c - u\| < 2$ m/s	0.500
$\|c - u\| < 1$ m/s	0.100

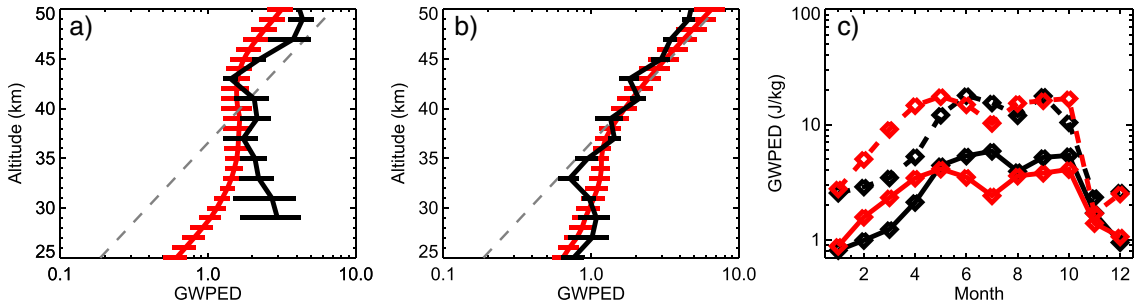

Figure 9. (a) Observed (black) and modeled monthly mean GWPED profile (red) for November 2011. Horizontal bars mark the standard deviation of the mean. The dashed line shows the conservative growth rate. (b) Same as Figure 9a but for December 2011. (c) Annual oscillation of the GWPED in 30–40 km (solid lines) and 40–50 km altitude (dashed lines).

is found by comparing the annual oscillation in GWPED observed by lidar with model results. Note that the very same scaling factor is applied to all model data.

Figure 9 shows model results as well as corresponding lidar observations. It is evident from this figure that the model reproduces the approximate altitude regions where filtering of waves takes place, i.e., altitudes where GWPED profiles deviate from the conservative growth rate. Also, total dissipation in the model matches the observations in December (Figure 9b) quite well, and energy densities at 25 km altitude and above 37 km altitude agree within one standard deviation. In November (Figure 9a) the total dissipation is underestimated by approximately 50%. However, large uncertainty estimates of measured GWPED below 32 km make dissipation estimates unreliable. A good agreement between observations and model is found for altitudes above 34 km. Figure 9c shows observed and modeled annual oscillations in GWPED. Significant seasonal variations are captured by the model. In particular, the double-humped structure of the winter maximum is reproduced for both altitude ranges, although in model data the local minimum in July precedes the observations by 1 month. We note that in late summer/autumn (months February–April) the GWPED in our model increases much faster compared to observations. On the other hand, the sharp decrease in GWPED caused by the breakdown of the polar vortex is well reproduced.

6. Discussion

The gravity wave measurements in the stratosphere obtained by the IAP iron lidar can be compared with results from other instruments on the Antarctic continent. GWPED measurements in the Antarctic region have been published in several recent studies. The study by *Alexander et al.* [2011] is based on 839 h of Rayleigh lidar measurements at Davis Station acquired during the winters of March–October 2007 and March–September 2008. The instrument was colocated with our lidar, and the results are thus predestined for comparisons. *Yamashita et al.* [2009] discuss GWPED measured by an iron Boltzmann lidar at Rothera (67.5°S, 68.0°W) and at the South Pole. This is so far the only previous lidar-based study which covers all 12 months throughout a year. Because of 24 h of daylight, lidar observations in polar summer are, in general, difficult and require special narrowband optical filter. From December 2002 to March 2005 the Boltzmann lidar was located at Rothera and operated for 507 h [*Yamashita et al.*, 2009]. The second group of GWPED measurements are based on radiosonde soundings. *Moffat-Griffin et al.* [2011] analyzed an 8 year series of 965 soundings over Rothera and published a gravity wave climatology. *Yoshiki et al.* [2004] show GWPED results from twice daily soundings over Syowa Station (69.0°S, 39.6°E) for the time frame February 1997 to January 1999.

Vertical GWPED profiles published by *Alexander et al.* [2011] are shown in Figure 4. Given that the lidar observations were carried out before the IAP iron lidar was installed at Davis and therefore do not overlap in time with our measurements, differences between the two winter profiles are surprisingly small. In fact, variations between our results and the GWPED profile published by *Alexander et al.* [2011] amount to less than 5% for altitudes below 47 km. Differences in the autumn profiles are slightly larger (approximately 20%). The largest part of these differences can be attributed to a horizontal shift of the two profiles. Because there are relatively few measurement hours in March, our autumn GWPED profile is likely biased toward the winter state, i.e., the profile is shifted toward larger values. Taking this bias into account, again there is a surprisingly good agreement between our results and the lidar measurements collected 4 years earlier.

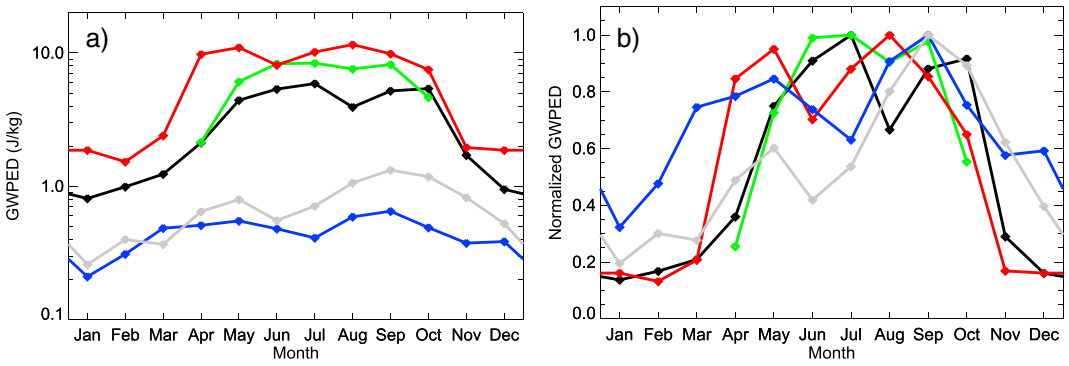

Figure 10. (a) Seasonal variations of monthly mean GWPED at Davis: black: 30–40 km (this work) and green: 37 km [from *Alexander et al.*, 2011]. Rothera: red: 30–45 km [from *Yamashita et al.*, 2009] and blue: 15–22 km [from *Moffat-Griffin et al.*, 2011]. Syowa: gray: 20–22 km [from *Yoshiki et al.*, 2004]. (b) Same as Figure 10a with maxima of traces scaled to unity. See text for details.

In order to compare seasonal variations in GWPED with our results, we digitized and processed data published in previous studies. The processing was done as follows: First, we computed monthly means from daily [*Alexander et al.*, 2011] and weekly averages [*Yamashita et al.*, 2009]. In the case of *Yoshiki et al.* [2004] we computed monthly means from the digitized time series. Figure 10a shows the resulting climatologies. While lidars generally observe stratospheric gravity waves in the range 30–50 km, radiosonde soundings are limited to much lower altitudes. To compare the different observations in terms of seasonal variations, in a second step we removed the altitude dependence of the GWPED (the GWPED grows approximately exponentially with altitude) by scaling each trace such that the maximum equals unity. The normalized traces (Figure 10b) show several interesting features: (1) The annual oscillations of the GWPED in the upper stratosphere at Davis and Rothera (black and red line) are almost identical with same values in summer and similar peak values in winter. (2) All observations show a double-humped structure with a dip around midwinter. At Rothera and Syowa the dip occurs earlier (June/July) than at Davis (August). (3) In the lower stratosphere the first winter maximum is smaller than the second maximum (gray and blue lines), while maxima of equal height are observed in the upper stratosphere (black and red lines). Also, the summer/winter and winter/summer transitions are more gradual in the lower stratosphere.

Quantitative comparisons are often hindered by research groups using different analysis and gravity wave extraction techniques or simply by publishing results which are averaged over different altitude ranges. Nonetheless, our GWPED measurements are comparable in magnitude and show generally the same seasonal variations. Minimum gravity wave activity occurs in January which is in agreement with the Syowa and Rothera radiosonde measurements. Only the Rothera lidar-based data set shows a minimum in February, 1 month later than the other data sets. The good agreement between the data sets is even more surprising given that data were recorded in different years. This suggests very stable atmospheric conditions in summer with little year-to-year variation and similar gravity wave transmission characteristics across the Antarctic continent. Davis (78°E) and Rothera (68°W) are nearly opposite to each other with respect to the South Pole. Moreover, all data sets show a rapid decrease in GWPED correlated with the breakdown of the polar vortex in months October and November. In accordance with the reversal of the zonal wind progressing downward during these months, the decrease in GWPED happens faster for lidar-based measurements in the upper stratosphere. Radiosonde-based observations show a more gradual decrease because radiosondes are limited to the lower stratosphere and are thus farther away from the wind speed maximum of the polar jet.

The relative constancy of the circulation in the Antarctic and the small interannual variability in GWPED found in this study are characteristics of the Southern Hemisphere. By contrast, the circulation in the Arctic is much more variable. In winter, the abrupt deceleration of the zonal wind associated with sudden stratospheric warmings can even cause reversal of the mean flow [*Matsuno*, 1971]. Such drastic changes to the wind field and thermal structure affect the generation and propagation of gravity waves. As a result, at northern middle to high latitudes gravity wave activity shows a significant interannual variability. For example, *Thurairajah et al.* [2010] report for three consecutive winter seasons (Chatanika; 65°N, 147°W) average stratospheric GWPED values 2.1 J/kg, 1.1 J/kg, and 5.7 J/kg. Interannual variability of approximately half an order of magnitude is also evident in long-term lidar observations at Esrange (68°N, 21°E) [*Ehard et al.*, 2014]. Differences in gravity

wave activity between the Northern and Southern Hemispheres are also likely candidates to explain observed interhemispheric differences in polar mesospheric summer echoes and noctilucent clouds [*Morris et al.*, 2009; *Kaifler et al.*, 2013].

We studied the influence of the polar jet on gravity wave propagation based on a very simplistic model in section 5. Despite all the obvious shortcomings and oversimplifications, the GWPED climatology produced by the model agrees surprisingly well with our lidar observations. This leads us to the conclusion that major seasonal variations in gravity wave activity are caused by filtering of waves in the lower stratosphere. More specifically, we postulate that the gravity wave flux observed in the middle atmosphere is largely independent of variations in the tropospheric source region or modulations of the strength and characteristics of the sources. Tropospheric sources may emit waves with different spectral characteristics. However, most of this variability is lost once waves pass through the lower stratosphere which acts as a selective filter. The spectral shape of the sources is thus less significant as long as the sources are on average spectrally broad enough to cover the passband of the stratospheric filter. This insensitivity to spectral characteristics is the main reason the simplistic model works so well in reproducing the observed seasonal oscillation in GWPED.

Modulation of gravity wave activity by winds has been investigated in previous studies [*Wilson et al.*, 1991; *Thurairajah et al.*, 2010]. *Wilson et al.* [1991] noted the correlation between gravity wave energies and wind speed. They concluded that the atmosphere could act as a selective filter for gravity waves and the filtering process could induce a seasonal variability in gravity wave activity in the middle atmosphere. The work by *Wilson et al.* [1991] is based on lidar observations at a midlatitude site. For Davis, the selective filtering of waves plays an even more important role because Davis is at high latitudes and thus closer to the wind speed maximum of the polar jet. The upper stratosphere over Davis in winter as well as in summer is characterized by zonal wind speeds increasing with altitude (see Figure 7). Gravity waves with small phase speeds are thus far from encountering critical levels in this region. Filtering of waves takes place predominantly in the tropopause region where wind speeds are lowest. Consequently, low-speed waves which penetrate into the upper stratosphere in winter or summer are likely to propagate freely until the wave spectrum becomes saturated and wave breaking sets in. *Alexander et al.* [2011] published evidence for conservative wave propagation over Davis in winter between 35 and 39 km altitude. Our measurements confirm GWPED growth rates which are compatible with free wave propagation between 29 and 40 km (Figure 4). Moreover, excellent agreement is found between the two data sets in the overlapping region (39–49 km), and both data sets show first signs of wave breaking around 42 km. This suggests very little year-to-year variation in gravity wave activity in the winter upper stratosphere, given that measurements were carried out in different years. Consequently, we conclude that either variability of gravity wave sources is also small in winter or this variability is effectively removed by selective filtering of gravity waves in the lower stratosphere/upper troposphere.

Since our lidar data cover two summer seasons, we can use the large number of observations (590 observation hours in total) to estimate the precision of our summer GWPED profile. Assuming conservative wave propagation between 29 and 43 km, GWPED grows proportional to $\exp(z/h)$. Fitting this exponential to our data yields a goodness of fit χ^2 value which summarizes the discrepancy between our data and the model (exponential growth). Using the standard deviation of the mean as uncertainty estimate yields $\chi^2 = 0.24$. This suggests that the standard deviation of the mean overestimates the true uncertainty of the mean. One likely explanation is non-Gaussian distributed natural variability in gravity wave activity. Only if we reduced the uncertainty estimates by a factor 4.3 we were able to achieve a χ^2 value of close to unity. This translates to a true relative uncertainty in our summer GWPED profile of less than 2.7%. In other words, our measurements are compatible with a constant GWPED growth rate indicative of conservative wave propagation if we assume measurement uncertainties as small as 2.7%. Note that this value applies only to the summer mean profile. Uncertainties of individual observational means are generally larger.

Even though waves start to break near the stratopause, temperature perturbation amplitudes generally increase with height throughout the upper stratosphere and mesosphere. This assumption appears to be valid also for individual waves in a partitioned phase speed spectrum. In section 5 we discussed the influence of the zonal wind on filtering selectively gravity waves with certain phase speeds. As we cannot measure the phase speed of waves directly, we rely on the GWPED as diagnostic tool. We showed in Figure 8 that the GWPED is strongly reduced in regions of heights where the zonal wind speed is close to zero. The correlation suggests filtering of waves with small phase speeds in these regions because waves removed from the phase speed spectrum do not contribute to the GWPED anymore. This has important consequences for the gravity wave

flux in the stratosphere as well as in the mesosphere. In the absence of additional wave sources and nonlinear wave-wave interactions, gaps once created in the phase speed spectrum persist all the way up through the atmosphere. As a result, selective filtering of gravity waves in the lower stratosphere reduces the wave flux (GWPED) not only in the upper stratosphere but also in the mesosphere. The vertical coupling is clearly visible in Figure 6. During winter months June–October GWPED values in the stratosphere are strongly correlated with those in the mesosphere. In particular, the dips in August are comparable in magnitude. The dip separating the two winter peaks also appears in our model results (Figure 9) although shifted by 1 month. Inspection of the ECMWF zonal wind data reveals that the reduction in GWPED results from selective filtering of gravity waves near the tropopause level. Most likely, this is also the case for the measurement data showing the dip in August. Thus, the combination of model results and lidar observations demonstrates that the gravity wave flux (GWPED) in the MLT region is effectively controlled by the structure of the zonal wind in the tropopause region and lower stratosphere. In summer the situation is more complicated. Fluctuations in wind speed also likely modulate the wave flux. However, the modulation has little effect on the MLT region because the zonal wind reverses in the stratosphere, thus blocking all gravity waves with small phase speeds. According to this, the GWPED peak in summer must result from waves with larger phase speeds which penetrate through the stratosphere mostly unaffected. The result is a characteristic semiannual oscillation previously reported by *Hoffmann et al.* [2010]. One notable exception is the smaller peak in March. Studying the structure of the zonal wind reveals a short period in the beginning of March which is characterized by low positive wind speeds throughout the stratosphere and lower mesosphere. The contour lines in Figure 7 run almost vertically during this period. Consequently, gravity waves with small phase speeds are able to propagate deeply into the mesosphere, while before and after this period these waves are filtered. The increased wave flux reaching the MLT region causes the GWPED enhancement in March which is not seen in the stratosphere. *Dowdy et al.* [2007] published a gravity wave climatology for the Davis MLT region based on multiyear MF radar observations. Because the climatology does not show any enhancement in the relevant period, we conclude that the GWPED peak in March is most likely the result of sporadic events which do not occur every year.

7. Summary and Conclusion

In this work, we analyze lidar observations made at the Antarctic research station Davis for gravity waves. We use the gravity wave potential energy density (GWPED) as proxy for wave activity and study vertical propagation of waves as well as selective filtering of waves due to critical levels caused by the structure of the zonal wind.

We find a clear annual oscillation in gravity wave activity showing a broad double maximum in winter. The seasonal variation is similar in both the midstratosphere (30–40 km) and the upper mesosphere (85–95 km). Variations in gravity wave activity in the stratosphere are correlated with zonal wind and can be modeled as variations due to critical layer filtering by the wind. The seasonal behavior in gravity wave activity is remarkably similar across the Antarctic continent. Interannual variations are smaller than in the Northern Hemisphere.

The correlation between gravity wave activity in the stratosphere and upper mesosphere suggest that the wavefield in the mesosphere is dominated by waves propagating from below. In comparing model results with observations we find that most of the wave filtering takes place in the lower stratosphere; i.e., the wind field in the lower stratosphere essentially controls the gravity wave flux in the upper mesosphere.

The extensive lidar data set will enable more detailed investigations of gravity wave parameters in the stratosphere as well as the mesosphere. Such studies will be important for understanding deep gravity wave propagation and effects resulting from the coupling between the troposphere, stratosphere, mesosphere, and lower thermosphere. The studies may also contribute to the understanding of gravity wave-related phenomenon such as structures in polar mesospheric clouds and the occurrence of polar mesospheric summer echoes.

Acknowledgments
We would like to thank the Australian Antarctic Division for logistics and support in carrying out lidar measurements at Davis Station. ECMWF data used in this study have been obtained from the ECMWF data server. Lidar data are archived by the Leibniz Institute of Atmospheric Physics and are available on request from www.iap-kborn.de. Analysis methods used to extract gravity wave parameters are described in the text.

References

Alexander, M. J., et al. (2008), Global estimates of gravity wave momentum flux from High Resolution Dynamics Limb Sounder observations, *J. Geophys. Res.*, *113*, D15S18, doi:10.1029/2007JD008807.

Alexander, S. P., A. R. Klekociuk, and D. J. Murphy (2011), Rayleigh lidar observations of gravity wave activity in the winter upper stratosphere and lower mesosphere above Davis, Antarctica (69°S, 78°E), *J. Geophys. Res.*, *116*, D13109, doi:10.1029/2010JD015164.

Allen, S. J., and R. A. Vincent (1995), Gravity wave activity in the lower atmosphere: Seasonal and latitudinal variations, *J. Geophys. Res.*, *100*(D1), 1327–1350, doi:10.1029/94JD02688.

Andrews, D., J. Holton, and C. Leovy (1987), *Middle Atmosphere Dynamics*, Academic Press, Orlando, Fla.

Becker, E. (2012), Dynamical control of the middle atmosphere, *Space Sci. Rev.*, *168*, 283–314, doi:10.1007/s11214-011-9841-5.

Chen, C., X. Chu, A. J. McDonald, S. L. Vadas, Z. Yu, W. Fong, and X. Lu (2013), Inertia-gravity waves in Antarctica: A case study using simultaneous lidar and radar measurements at McMurdo/Scott Base (77.8°S, 166.7°E), *J. Geophys. Res. Atmos.*, *118*, 2794–2808, doi:10.1002/jgrd.50318.

Collins, R., and C. Gardner (1995), Gravity wave activity in the stratosphere and mesosphere at the South Pole, *Adv. Space Res.*, *16*(5), 81–90, doi:10.1016/0273-1177(95)00175-E.

Dowdy, A. J., R. A. Vincent, M. Tsutsumi, K. Igarashi, Y. Murayama, W. Singer, and D. J. Murphy (2007), Polar mesosphere and lower thermosphere dynamics: 1. Mean wind and gravity wave climatologies, *J. Geophys. Res.*, *112*, D17104, doi:10.1029/2006JD008126.

Duck, T. J., J. A. Whiteway, and A. I. Carswell (2001), The gravity wave-Arctic stratospheric vortex interaction, *J. Atmos. Sci.*, *58*, 3581–3596, doi:10.1175/1520-0469(2001)058<3581:TGWASV>2.0.CO;2.

Ehard, B., P. Achtert, and J. Gumbel (2014), Long-term lidar observations of wintertime gravity wave activity over northern Sweden, *Ann. Geophys.*, *32*(11), 1395–1405, doi:10.5194/angeo-32-1395-2014.

Fritts, D. C., and L. Yuan (1989), An analysis of gravity wave ducting in the atmosphere: Eckart's resonances in thermal and Doppler ducts, *J. Geophys. Res.*, *94*(D15), 18,455–18,466, doi:10.1029/JD094iD15p18455.

Gardner, C. S., X. Chu, P. J. Espy, J. M. C. Plane, D. R. Marsh, and D. Janches (2011), Seasonal variations of the mesospheric Fe layer at Rothera, Antarctica (67.5°S, 68.0°W), *J. Geophys. Res.*, *116*, D02304, doi:10.1029/2010JD014655.

Gerrard, A. J., T. J. Kane, J. P. Thayer, and S. D. Eckermann (2004), Concerning the upper stratospheric gravity wave and mesospheric cloud relationship over Søndrestrøm, Greenland, *J. Atmos. Sol. Terr. Phys.*, *66*(3–4), 229–240, doi:10.1016/j.jastp.2003.12.005.

Hoffmann, P., E. Becker, W. Singer, and M. Placke (2010), Seasonal variation of mesospheric waves at northern middle and high latitudes, *J. Atmos. Sol. Terr. Phys.*, *72*(14–15), 1068–1079, doi:10.1016/j.jastp.2010.07.002.

Holton, J. R. (1983), The influence of gravity wave breaking on the general circulation of the middle atmosphere, *J. Atmos. Sci.*, *40*(10), 2497–2507, doi:10.1175/1520-0469(1983)040<2497:TIOGWB>2.0.CO;2.

Kaifler, N., G. Baumgarten, A. Klekociuk, S. Alexander, J. Fiedler, and F.-J. Lübken (2013), Small scale structures of NLC observed by lidar at 69°N/69°S and their possible relation to gravity waves, *J. Atmos. Sol. Terr. Phys.*, *104*, 244–252, doi:10.1016/j.jastp.2013.01.004.

Klekociuk, A., M. Lambert, R. Vincent, and A. Dowdy (2003), First year of Rayleigh lidar measurements of middle atmosphere temperatures above Davis, Antarctica, *Adv. Space Res.*, *32*(5), 771–776, doi:10.1016/S0273-1177(03)00421-6.

Lautenbach, J., and J. Höffner (2004), Scanning iron temperature lidar for mesopause temperature observation, *Appl. Opt.*, *43*(23), 4559–4563, doi:10.1364/AO.43.004559.

Lindzen, R. S. (1981), Turbulence and stress owing to gravity wave and tidal breakdown, *J. Geophys. Res.*, *86*(C10), 9707–9714, doi:10.1029/JC086iC10p09707.

Lübken, F.-J. (1999), Thermal structure of the Arctic summer mesosphere, *J. Geophys. Res.*, *104*(D8), 9135–9149, doi:10.1029/1999JD900076.

Lübken, F.-J., J. Höffner, T. P. Viehl, B. Kaifler, and R. J. Morris (2014), Winter/summer mesopause temperature transition at Davis (69°S) in 2011/2012, *Geophys. Res. Lett.*, *41*, 5233–5238, doi:10.1002/2014GL060777.

Lue, H. Y., F. S. Kuo, S. Fukao, and T. Nakamura (2013), Studies of gravity wave propagation in the mesosphere observed by MU radar, *Ann. Geophys.*, *31*(5), 845–858, doi:10.5194/angeo-31-845-2013.

Matsuno, T. (1971), A dynamical model of the stratospheric sudden warming, *J. Atmos. Sci.*, *28*(8), 1479–1494, doi:10.1175/1520-0469(1971)028<1479:ADMOTS>2.0.CO;2.

Moffat-Griffin, T., R. E. Hibbins, M. J. Jarvis, and S. R. Colwell (2011), Seasonal variations of gravity wave activity in the lower stratosphere over an Antarctic Peninsula station, *J. Geophys. Res.*, *116*, D14111, doi:10.1029/2010JD015349.

Morris, R. J., A. R. Klekociuk, R. Latteck, W. Singer, D. A. Holdsworth, and D. J. Murphy (2009), Inter-hemispheric asymmetry in polar mesosphere summer echoes and temperature at 69° latitude, *J. Atmos. Sol. Terr. Phys.*, *71*(3–4), 464–469, doi:10.1016/j.jastp.2008.09.042.

Nicolls, M. J., R. H. Varney, S. L. Vadas, P. A. Stamus, C. J. Heinselman, R. B. Cosgrove, and M. C. Kelley (2010), Influence of an inertia-gravity wave on mesospheric dynamics: A case study with the Poker Flat Incoherent Scatter Radar, *J. Geophys. Res.*, *115*, D00N02, doi:10.1029/2010JD014042.

Nomura, A., Y. Iwasaka, and T. Kano (1989), Gravity wave activities over Syowa Station, Antarctica, in *Proc. of the NIPR Symposium on Polar Meteorology and Glaciology*, vol. 2, edited by T. Hoshiai, pp. 1–7, Nat'l. Inst. of Polar Res., Tokyo.

Olivero, J. J., and G. E. Thomas (1986), Climatology of polar mesospheric clouds, *J. Atmos. Sci.*, *43*(12), 1263–1274, doi:10.1175/1520-0469(1986)043<1263:COPMC>2.0.CO;2.

Rapp, M., and G. E. Thomas (2006), Modeling the microphysics of mesospheric ice particles: Assessment of current capabilities and basic sensitivities, *J. Atmos. Sol. Terr. Phys.*, *68*(7), 715–744, doi:10.1016/j.jastp.2005.10.015.

Rauthe, M., M. Gerding, and F.-J. Lübken (2008), Seasonal changes in gravity wave activity measured by lidars at mid-latitudes, *Atmos. Chem. Phys.*, *8*(22), 6775–6787, doi:10.5194/acp-8-6775-2008.

Thurairajah, B., R. L. Collins, V. L. Harvey, R. S. Lieberman, and K. Mizutani (2010), Rayleigh lidar observations of reduced gravity wave activity during the formation of an elevated stratopause in 2004 at Chatanika, Alaska (65°N, 147°W), *J. Geophys. Res.*, *115*, D13109, doi:10.1029/2009JD013036.

Wang, L., and M. J. Alexander (2010), Global estimates of gravity wave parameters from GPS radio occultation temperature data, *J. Geophys. Res.*, *115*, D21122, doi:10.1029/2010JD013860.

Wilson, R., M. L. Chanin, and A. Hauchecorne (1991), Gravity waves in the middle atmosphere observed by Rayleigh lidar: 2. Climatology, *J. Geophys. Res.*, *96*(D3), 5169–5183, doi:10.1029/90JD02610.

Wright, C. J., and J. C. Gille (2013), Detecting overlapping gravity waves using the S-Transform, *Geophys. Res. Lett.*, *40*, 1850–1855, doi:10.1002/grl.50378.

Yamashita, C., X. Chu, H.-L. Liu, P. J. Espy, G. J. Nott, and W. Huang (2009), Stratospheric gravity wave characteristics and seasonal variations observed by lidar at the South Pole and Rothera, Antarctica, *J. Geophys. Res.*, *114*, D12101, doi:10.1029/2008JD011472.

Yoshiki, M., N. Kizu, and K. Sato (2004), Energy enhancements of gravity waves in the Antarctic lower stratosphere associated with variations in the polar vortex and tropospheric disturbances, *J. Geophys. Res.*, *109*, D23104, doi:10.1029/2004JD004870.

Yu, Z., X. Chu, W. Huang, W. Fong, and B. R. Roberts (2012), Diurnal variations of the Fe layer in the mesosphere and lower thermosphere: Four season variability and solar effects on the layer bottomside at McMurdo (77.8°S, 166.7°E), Antarctica, *J. Geophys. Res.*, *117*, D22303, doi:10.1029/2012JD018079.

Zhang, F. (2004), Generation of mesoscale gravity waves in upper-tropospheric jet-front systems, *J. Atmos. Sci.*, *61*(4), 440–457, doi:10.1175/1520-0469(2004)061<0440:GOMGWI>2.0.CO;2.